Structural Dynamics ARTICLE scitation.org/journal/sdy

Time-resolved diffraction with an optimized short pulse laser plasma X-ray source

Cite as: Struct. Dyn. 7, 014301 (2020); doi: 10.1063/1.5126316
Submitted: 1 September 2019 · Accepted: 16 December 2019 ·
Published Online: 2 January 2020

View Online Export Citation CrossMark

M. Afshari, P. Krumey, D. Menn, M. Nicoul, F. Brinks, A. Tarasevitch, and K. Sokolowski-Tinten[a)]

AFFILIATIONS

Faculty of Physics and Center for Nanointegration Duisburg-Essen, University of Duisburg-Essen, Lotharstrasse 1, 47048 Duisburg, Germany

[a)]Klaus.Sokolowski-Tinten@uni-due.de

ABSTRACT

We present a setup for time-resolved X-ray diffraction based on a short pulse, laser-driven plasma X-ray source. The employed modular design provides high flexibility to adapt the setup to the specific requirements (e.g., X-ray optics and sample environment) of particular applications. The configuration discussed here has been optimized toward high angular/momentum resolution and uses K_α-radiation (4.51 keV) from a Ti wire-target in combination with a toroidally bent crystal for collection, monochromatization, and focusing of the emitted radiation. 2×10^5 Ti-$K_{\alpha 1}$ photons per pulse with 10^{-4} relative bandwidth are delivered to the sample at a repetition rate of 10 Hz. This allows for the high dynamic range (10^4) measurements of transient changes in the rocking curves of materials as for example induced by laser-triggered strain waves.

© 2019 Author(s). All article content, except where otherwise noted, is licensed under a Creative Commons Attribution (CC BY) license (http://creativecommons.org/licenses/by/4.0/). https://doi.org/10.1063/1.5126316

I. INTRODUCTION

Combining atomic scale spatial and temporal resolution ultrafast time-resolved diffraction using short X-ray or electron pulses provides direct access to atomic motions in materials on their natural time scale, i.e., femtoseconds to picoseconds. This relatively new field of "structural dynamics" has seen tremendous progress in recent years mainly driven by the development of new sources (e.g., Refs. 1–4 and references therein). In the case of X-rays, the current standard is set by X-ray free electron lasers, which exhibit extreme brightness, ultrashort pulse duration (currently down to the few femtosecond level), and spatial coherence offering spectacular new opportunities.[5] While more and more of these large-scale facilities are getting operational and available to users, access is highly competitive and still very limited. Therefore, as an alternative, lab-scale approaches are still being pursued and developed. Among these, the hard X-ray emission of short-pulse laser-produced plasmas has found wide-spread use for radiography/imaging (e.g., Refs. 6–8), time-resolved X-ray absorption (e.g., Refs. 9–13), and, in particular, ultrafast diffraction (e.g., Refs. 14–24). In fact, the first time-resolved X-ray diffraction experiment with subpicosecond resolution has been performed at such a source.[25]

By focusing a femtosecond laser pulse at intensities in excess of 10^{16} Wcm^{-2} onto the surface of a solid target, high temperature plasmas with near-solid-density can be generated,[26] which represent an efficient source of hard X-rays.[27,28] The emitted radiation contains continuum and characteristic line emission from the thin surface plasma layer and the "cold" solid behind. Due to collisionless interactions[29–37] (resonance absorption and/or vacuum heating) between the created plasma and the laser pulse, a fraction of the plasma electrons is accelerated to kinetic energies of several tens of kilo-electron-volts, much higher than the thermal energy of the rest of the plasma electrons (several hundreds of electron volts).[38] These "hot" electrons generate Bremsstrahlung and characteristic line emission very similar to a conventional X-ray tube by penetrating into the cold solid underneath the plasma layer. Since these high energy, hot electrons are a result of the direct laser-plasma interaction, the X-ray pulse duration can be comparable to the driving laser pulse duration.[34,39]

The efficiency of X-ray production critically depends on the hot electron distribution (their energy and number) and thus on the details of the laser-plasma interaction, which can be controlled through the laser parameters such as wavelength, intensity, angle of incidence, and laser polarization, as well as the properties of the created plasma (e.g., scale length).

For example, the K-shell ionization cross section is maximum at electron energies of a few times the K-shell ionization energy of a given material.[40] Consequently, optimum K_α production can be expected if the average energy of the hot electron distribution peaks in this

range.[34,41,42] This average energy, often described by an effective hot electron temperature T_h, scales with the ponderomotive energy, i.e., $T_h \propto I_0 \cdot \lambda^2$, where I_0 is the laser intensity and λ its wavelength.[43–46] Therefore, the laser wavelength and laser intensity are control parameters to improve the efficiency of X-ray production[47] or to push the X-ray emission to higher energies.[48–50]

Similarly important is the plasma scale length reached at the peak of the laser pulse where the intensity is maximum.[30] Since plasma formation occurs already at intensities in the range of 10^{13} Wcm^{-2}, the conversion efficiency is very sensitive to the temporal structure of the rising edge of the laser pulse. If the laser-pulse contrast ratio (LPCR) is low (e.g., due to imperfect stretching and recompression of the laser pulses in the typically used chirped-pulse-amplification—CPA—laser systems or due to prepulses and/or amplified spontaneous emission—ASE), plasma formation and expansion occur well before the pulse maximum. In some cases,[35,36,51,52] a "passive" optimization of X-ray production has been achieved through the inherent time structure of the given drive laser. In contrast, laser systems with high LPCR controlled prepulse schemes have been employed to actively improve laser-driven plasma X-ray sources.[42,53–57]

Based on our previous detailed investigations of K_α X-ray production,[57] we present here a setup for time-resolved X-ray diffraction based on an optimized laser-driven plasma Ti-K_α X-ray source. We employ a modular design that provides high flexibility with respect to the specific requirements (e.g., X-ray optics and sample environment) of particular applications. The configuration discussed here has been optimized toward high angular/momentum resolution by using a toroidally bent crystal for collection, monochromatization, and focusing of the emitted radiation.

This paper is organized as follows: In Sec. II, we give a brief description of the technical features of the setup. The main section discusses the spectral characterization of the X-ray source (Sec. III A), the optimization of its K_α yield (Sec. III B), the characterization of the toroidally bent crystal used for focusing and monochromatization (Sec. III C), and static and time-resolved diffraction experiments on "test" samples to demonstrate its performance (Sec. III D). Finally, Sec. IV summarizes the properties of the setup.

II. EXPERIMENTAL REALIZATION

The laser used as the driver for the X-ray source is a home-build CPA Ti:sapphire laser system, including an oscillator, an eight-pass preamplifier, and a four-pass booster amplifier. The system provides pulses with <100 fs pulse duration at a center wavelength of 800 nm and a pulse energy of approximately 150 mJ at a repetition rate of 10 Hz. The pulses exhibit a high LPCR of about 10^7 at 2 ps ahead of the pulse peak; the LPCR to ASE is better than 10^8.

First, the incoming laser beam is split into a "main-pulse" and a weaker "prepulse" beam by using a mirror with a hole in the center ("holey-mirror") as a beam splitter. While the main-pulse represents the actual X-ray driver, the prepulse is used to generate a preplasma to enhance X-ray generation (see Sec. III B). After introducing a suitable delay, these two beams are recombined by a second holey-mirror beam splitter. Before, a third beam, which serves as the "pump pulse" to excite the sample under study (separate delay control), is split from the main-pulse by an off-center holey-mirror beam splitter.

Main- and prepulses are guided collinearly to a small vacuum chamber (see Fig. 1; pressure $\approx 10^{-2}$ mbar) and focused by a plano–concave lens with a focal length of 30 cm onto the surface of a Ti wire with a diameter of 250 μm. The beam diameters at the focus of the lens are 25 μm and 60 μm for main- and prepulses, respectively. With the given pulse energy, this results in maximum intensities on the wire of close to 10^{17} Wcm^{-2} for the main-pulse and $\approx 10^{15}$ Wcm^{-2} for the prepulse. Due to their high intensity, both pulses induce material ablation in the irradiated area, and a fresh target has to be provided for each laser pulse (pair). Therefore, the wire is continuously pulled over high-precision, ball-bearing mounted guides using a motor with adjustable torque installed outside the vacuum chamber, resulting in a positional stability of about ± 5 μm in all directions.

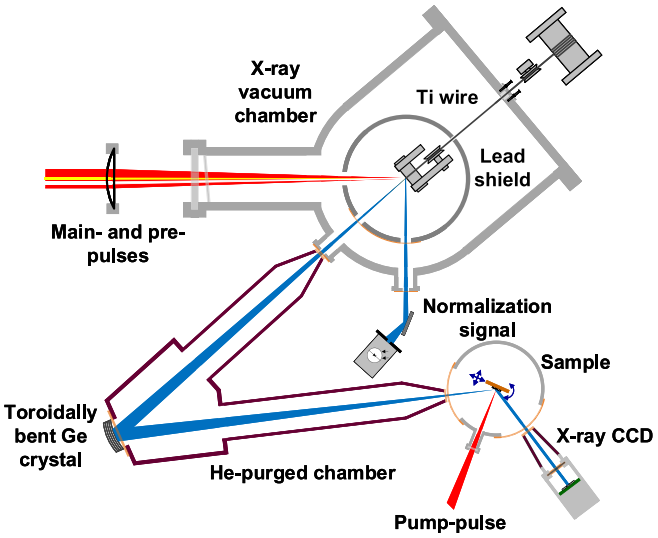

FIG. 1. Schematic of the optical-pump—X-ray-probe setup.

For radiation safety purposes and in order to eliminate any hard X-ray background, the wire-target assembly is enclosed by a lead-housing with minimized laser input and X-ray output openings. Additional lead shielding is attached to the inner walls of the stainless-steel vacuum chamber. Under normal operating conditions, this results in a radiation level below 1 μSv/h at 10 cm distance from the chamber.

As in a conventional X-ray tube, the X-ray emission of the plasma occurs spatially incoherent into the full solid angle. Therefore, suitable X-ray optics are required to collect and refocus the radiation of the plasma onto the sample under study. Here, we use a toroidally bent Ge crystal in a 1:1 imaging Rowland circle geometry.[58,59] The geometry is chosen such that the Bragg-condition is fulfilled over the whole area of the mirror resulting in very high reflectivity for a fraction of the bandwidth of the K_α-emission. As discussed in more detail below, a focus with a diameter of about 80 μm (FWHM), which contains up to 2×10^5 X-ray photons per pulse with a spectral bandwidth of approximately 0.43 eV centered on the $K_{\alpha 1}$ line, has been achieved at our source using this mirror.

With our modular scheme, only the X-ray source needs to be in vacuum to avoid nonlinearities in air due to the high intensity of the focused laser beam. The other parts of the setup (X-ray optic, sample

© Author(s) 2019

stage, and detector) are separated from the X-ray source chamber and can be flexibly moved/exchanged if required. For example, to enable experiments at low temperature, a cryostat with a small sample vacuum chamber can be inserted (as schematically depicted in Fig. 1). Alternatively, we use an in-air sample manipulator/goniometer for room-temperature measurements, which allows for larger or multiple samples. Since the Ti-K_α radiation at 4.51 keV is significantly absorbed in air (1/e absorption length $\approx$ 16 cm[60]), He-purged beam tubes are placed between different components to minimize absorption.

A thinned, back-illuminated Si CCD (Princeton Instrument PI-MTE:1300B) is used as a detector for the X-rays diffracted by the sample. This detector exhibits a quantum efficiency of 55% at 4.51 keV[61] and a chip area of 26.8 $\times$ 26 mm^2 (1340 $\times$ 1300 pixels of 20 $\times$ 20 μm^2 size).

To account for the variation of the X-ray flux due to both long-term drifts and short-term fluctuations,[62] a "direct" normalization[62–65] scheme has been implemented in which a GaAs crystal is properly placed at a second output of the X-ray source chamber, and the integrated diffraction signal of its (111)-reflection is monitored by a large area (diameter 10 mm) X-ray sensitive avalanche photodiode (APD). This allows us to normalize the diffraction signals recorded using the CCD with an accuracy of better than 2%.

The angle α between the optical pump and the X-ray probe beam in combination with the finite X-ray beam size leads to a variation in the relative arrival time at the sample surface limiting the temporal resolution of the experiment. For the current geometry ($\alpha \approx 50°$), this results in a temporal smearing of about 0.45 ps at a Bragg-angle of 20°, which reduces to 0.2 ps for larger Bragg-angles. This is still sufficient for the investigation of transient strain effects—the application this setup has been optimized for—which occur on "acoustic," picosecond time scales.

III. SETUP CHARACTERIZATION AND -OPTIMIZATION

This section discusses the detailed characterization and optimization of the setup. This includes the measurements of the source spectrum, our efforts to maximize the K_α yield, and the performance characterization of the bent crystal mirror in terms of efficiency, focusing capability, and bandwidth.

A. Spectral characterization

Spectral characterization has been done in two steps. First, the Si CCD was placed between the source and the bent crystal mirror and operated in photon-counting mode by drastically reducing the X-ray flux through a reduction of the drive laser power. In this mode, the detector acts as a spectrometer since a single X-ray photon produces a charge in the detecting pixel that is proportional to the photon energy.[66] Thus, a histogram of the signals in all the pixels of the CCD represents the spectrum of the detected radiation. A typical result is shown in Fig. 2(a).

The measured spectrum is characterized by a broad continuum and two line emission features, which represent the K_α and K_β emission of Ti. It needs to be stressed that the apparent continuum at energies below the K-shell emission lines is only partly due to Bremsstrahlung since at these photon energies, there is a non-negligible probability that the charge generated by a K_α or K_β photon is shared between two or more pixels.[66] Due to the limited energy resolution of about 150 eV, the CCD is not able to resolve spectral fine

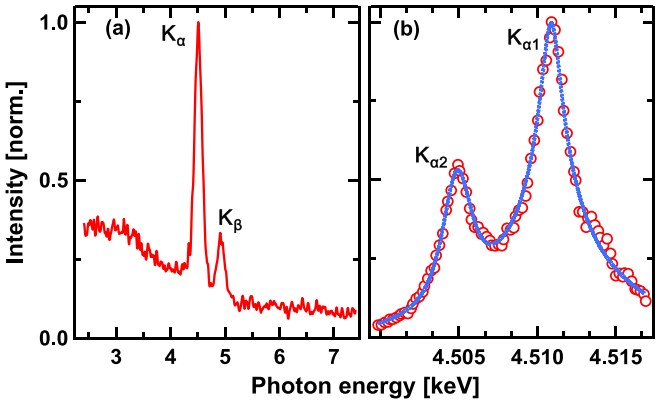

FIG. 2. Spectra of plasma X-ray emission: (a) low resolution spectrum measured using the X-ray CCD operating in photon counting mode. (b) High resolution spectrum of the Ti-K_α emission measured by rocking the toroidally bent mirror (red circles; the blue line represents a guide to the eye).

structures, namely, the spin–orbit split $K_{\alpha1}$ and $K_{\alpha2}$ lines (energy separation, 5.98 eV). Therefore, in a second step, the toroidally bent Ge crystal, which provides a spectral resolution of $\approx$ 0.43 eV (see Sec. III C), was utilized as a scanning spectrometer (by changing the incidence angle) to precisely measure the emitted K_α spectrum. As depicted in Fig. 2(b), the $K_{\alpha1}$ and $K_{\alpha2}$ lines are completely resolved. Their width was measured as $\approx$ 3.1 eV, which is broader than the reported natural Ti-K_α linewidths of about 1.45 eV and 2.13 eV,[67] respectively. This broadening has been observed before[68,69] and attributed to emission contributions from atoms in higher ionization states.

B. Source optimization

As discussed before, the drive laser intensity and the plasma scale length have a major influence on X-ray generation and thus the K_α-flux available in a diffraction experiment.

A straight-forward way to vary the intensity without changing the laser energy is to change the distance between the focusing lens and the wire, thus changing the laser spot size on the wire by moving it in and out of the focus, where the intensity is the highest. The red data points in Fig. 3(a) show the total K_α yield[70] as a function of the relative lens position (zero marks the position with the wire in the focus) for the case, when only the main-pulse is used for X-ray generation. It can be clearly seen that the maximum K_α yield is not obtained for the highest available intensity but with the wire approximately 0.4 mm before the focus and thus at an intensity below 10^{17} Wcm^{-2}. This is in agreement with previous observations[36,42,56,57,71] and also with the results of theoretical calculations[34] which predict a maximum K_α yield for Ti at intensities of a few times 10^{16} Wcm^{-2}.

Due to the high LPCR of the laser system used here, only a short scale length preplasma is created by the leading edge of a single pulse. Therefore, the collisionless coupling of laser energy to the plasma and consequently the X-ray production is not optimum.[30] We have shown previously[57] that it is possible to maximize the K_α flux by creating a preplasma with the angle of incidence-dependent optimum plasma scale length using a controlled prepulse with a suitable negative delay with respect to the X-ray generating main-pulse. We apply this approach here. The prepulse had a maximum intensity of almost 10^{15}

© Author(s) 2019

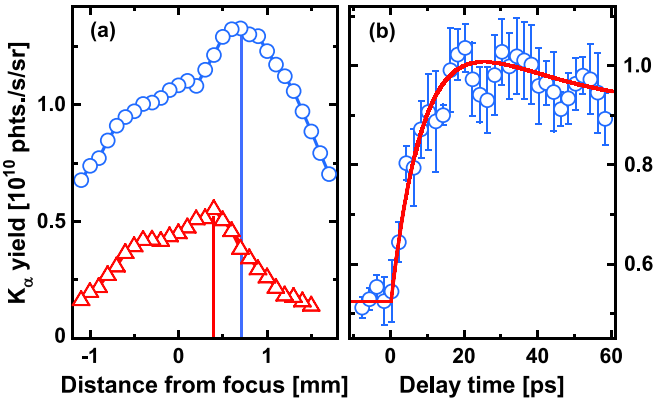

FIG. 3. Optimization of K_α X-ray production. (a) K_α yield as a function of the relative position of the laser focus with respect to the surface of the Ti wire, without (red triangles) and with (blue circles) prepulse [at optimum delay, see (b)]. (b) K_α yield as a function of delay time between pre- and main-pulses (blue circles; the red line is a guide to the eye).

Wcm^{-2} with the wire in the focus of the lens. The measured K_α yield vs delay time is depicted in Fig. 3(b). Positive delay times mean that the prepulse arrives earlier than the main-pulse, so the plasma scale length increases with delay time. As expected, the K_α flux is enhanced at positive delays, when the plasma generated by the prepulse has been expanded. A maximum yield increase of about a factor of two is reached at approximately 20 ps. In line with our previous results,[57] a relatively long scale length preplasma and thus a long delay between pre- and main-pulse are required due to the near-normal incidence of the laser on the wire, which has been chosen to minimize the effects of fluctuations of the wire position and the laser pointing.

The data shown in Fig. 3(b) have been measured at the lens position, which resulted in maximum K_α production "without" the prepulse.[72] As illustrated by the blue data points in Fig. 3(a), we were able to improve the X-ray yield with the prepulse further by reducing the intensity of both the pre- and the main-pulse through an increase in the wire-focus distance. At optimum conditions, a maximum Ti K_α flux of more than 1.3×10^{10} photons $s^{-1}sr^{-1}$ was achieved, which corresponds to $\approx 2 \times 10^5$ photons per pulse delivered to the sample.

C. X-Ray optics

Almost at any X-ray source, X-ray optical elements are used to direct, focus, or more generally manipulate the radiation for an intended application. For example, at accelerator based X-ray sources such as synchrotrons and X-ray free electron lasers, which usually exhibit well collimated and often highly monochromatic beams, lenses[73] and curved mirrors based on total reflection at grazing incidence[74] are employed. In contrast, the spatially incoherent 4π-emission of laser-plasma based X-ray sources requires optics, which allows us to collect the radiation over a sufficiently large solid angle and deliver it to the sample in a suitably shaped beam (focused and/or collimated). Bent crystals, multilayer mirrors, and capillary optics have been utilized for this purpose.[58,59,75–78]

Among these, bent crystals provide the highest spectral purity.[75] Since the spectral bandwidth determines the angular/momentum resolution of a diffraction experiment, such an optic has been chosen for the current setup. They are based on Bragg diffraction and can achieve a high reflectivity over a large area since the lattice planes are parallel to the geometrical surface of either spherically or toroidally bent crystals.[58]

In the current setup, we employ the (400)-reflection of a toroidally bent Ge-crystal with the (100)-orientation. It has been fabricated by INRAD, inc.,[79] to our specifications, and technical details have been discussed by Nicoul *et al.*[59] In brief, a 12.5 mm wide, 40 mm high, and 90 μm thick Ge crystal is bound to a toroidally shaped glass substrate [see the photograph in Fig. 4(a)]. Such a toroidally bent crystal mirror provides a quasimonochromatic 1:1 image of a point-like source if the source and image are located on the

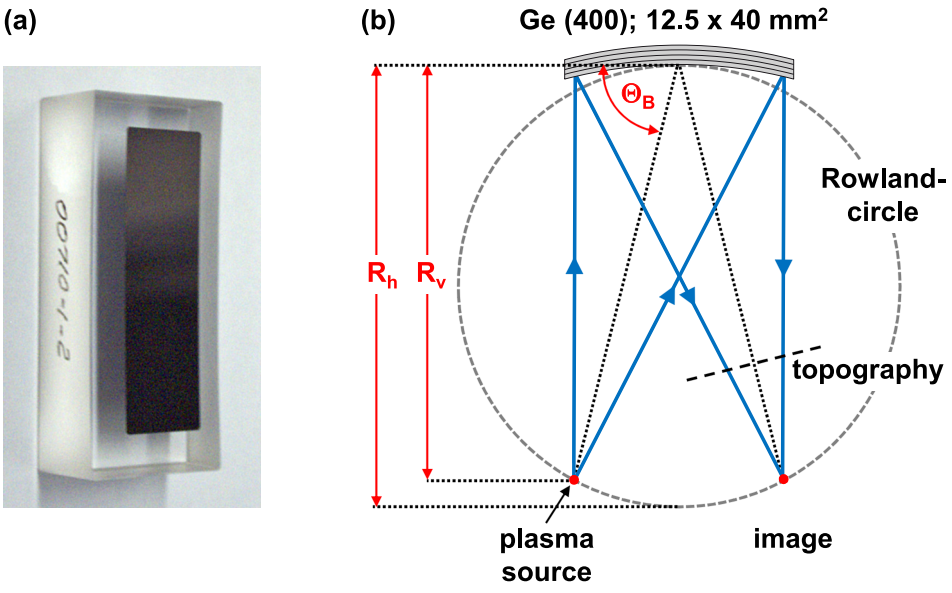

FIG. 4. (a) Photograph of the toroidally bent crystal X-ray mirror. (b) Schematic of the Rowland circle geometry resulting in a 1:1 imaging of the plasma source. The dashed line labeled topography marks the position of the X-ray CCD used to measure the reflectivity profile over the mirror surface [Fig. 5(a)].

© Author(s) 2019

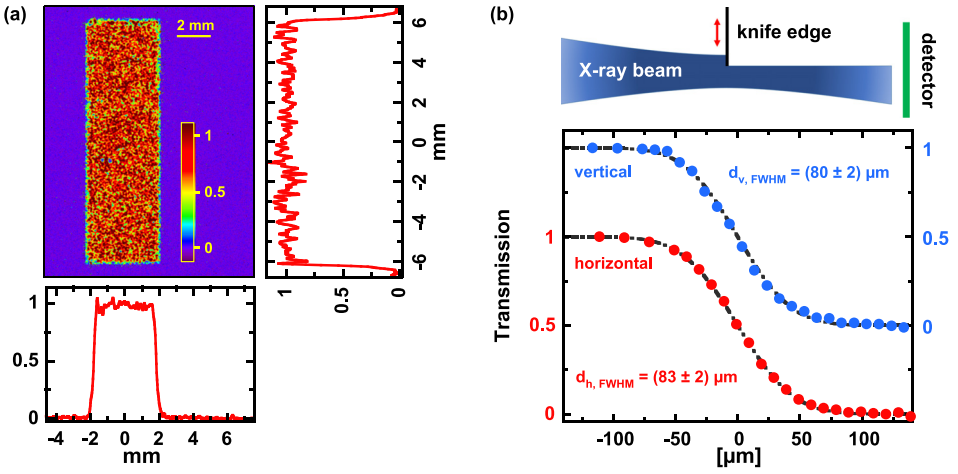

FIG. 5. (a) X-ray topography (spatial reflectivity distribution) of the bent crystal: False color image and vertical (right) and horizontal (bottom) cross sections. (b) Results of knife edge scans at the best focus position: Normalized $K_{\alpha 1}$ transmission as a function of vertical (blue) and horizontal (red) blade positions, respectively. The black dash-dotted curves represent error-function fits corresponding to Gaussian beam spot sizes (FWHM) noted in the graph.

so-called Rowland-circle, as depicted in Fig. 4(b), such that the vertical and horizontal bending radii R_V and R_H, respectively, satisfy the condition $\frac{R_V}{R_H} = \sin^2\theta_B$, with θ_B being the Bragg angle for the required X-ray wavelength (here, $\theta_B = 76.32°$ for Ti $K_{\alpha 1}$).

To ensure both the highest monochromaticity and a homogeneous reflectivity across the mirror surface, the source needs to be accurately positioned on the Rowland circle. Therefore, the source-mirror distance and the Bragg-angle [see also Fig. 2(b)] have been carefully adjusted by monitoring the intensity distribution of the reflected/diffracted K_α radiation with the X-ray CCD placed between the mirror and the sample/image position [marked by the dashed line labeled as "topography" in Fig. 4(b)]. Figure 5(a) shows the reflectivity distribution and its vertically and horizontally averaged cross sections for optimum adjustment. Despite fluctuations resulting from the short detector integration time (corresponding to a relatively low average number of photons per pixel), these data evidence a homogeneous reflectivity across the entire mirror surface. In the image plane ("focus" of the X-ray mirror), this transfers into a monochromatic and homogeneous intensity distribution as a function of angle over the full convergence range of 1.4° in the horizontal direction (the dispersion direction of our setup) and 4.5° vertically. In this configuration, the complete angular dependence of the diffraction signal of a sample, i.e., its rocking curve, can be obtained without actually "rocking" (rotating) the sample.

Another critical point for optical pump—X-ray probe experiments concerns the exact determination of the focus/image position of such a mirror because severe distortions of the angular distribution of the X-rays diffracted off the laser-excited area can occur if the sample under study is not properly positioned in the focus.[80] To precisely localize the focus, knife-edge scans using blades mounted on the sample stage exactly in the plane of the sample surface have been performed for different distances between the mirror and the sample [see the top schematic in Fig. 5(b)]. The results of such knife-edge scans for the best focus are depicted in the bottom part of Fig. 5(b), which shows the normalized "transmitted" signal as a function of the position of the horizontal (red) and vertical (blue) blades, respectively. The measured data can be described very well by an error function $T(x) = \frac{1}{2}(1 - erf(\frac{x}{x_0}))$ (black dash-dotted curves), where x_0 corresponds to the $1/e$-radius of a Gaussian beam. From these fits, we determine the focus/image diameter (FWHM) to 83 ± 2 μm and 80 ± 2 μm in horizontal and vertical directions, respectively. This size represents the convolution between the imaging properties of the bent mirror and the X-ray source size (which we have not measured here) and is small enough to allow for a sufficient pump-probe spot size ratio.

D. Static and Dynamic Diffraction

In this section, we present the results of static (without laser pumping) and time-resolved (with laser pumping) diffraction measurements to discuss the treatment of the diffraction data, to characterize the angular/momentum resolution of the experiment, and to demonstrate the overall performance and sensitivity of the setup. For this purpose, two different samples have been investigated, namely, a (100)-oriented bulk GaAs crystal and a 180 nm thick, (111)-oriented Ge film, hetero-epitaxially grown on a (111)-oriented bulk Si substrate.[81]

Figure 6(a) (top panel) shows the raw detector images of (i) the (400)-reflection of the GaAs crystal, (ii) the (111)-reflection of the Si substrate, and (iii) the (111)-reflection of the 180 nm thick Ge film on top of the Si crystal, all obtained with an integration time of 1 min (600 X-ray pulses) and without optical pumping. With an incident X-ray flux of about 2×10^5 K_α photons per pulse, the detected integrated diffraction signal in photons per pulse is 240, 90, and 60 for the GaAs (400), Si (111), and Ge (111) reflections, respectively.

All diffraction patterns exhibit the shape of curved lines [most pronounced for GaAs (400)]. This is caused by the fact that an X-ray "beam" with a large convergence (1.4° horizontally and 4.5° vertically) is used. As depicted schematically in Fig. 6(b), all possible incident and diffracted X-rays for a particular reflection (hkl) lie on the so-called Kossel-cone (blue), which has a full opening angle of $180° - 2\theta_B$ and an axis along the reciprocal lattice vector $\vec{G}_{hkl}$. From the Kossel-cone, the X-rays (with center ray $\vec{k}_X$) focused by the bent mirror onto the sample surface [marked green in Fig. 6(b)] cut out a curved, line-shaped segment (red). Since the opening angle of the Kossel-cone decreases with the increasing Bragg-angle, the curvature of the diffraction pattern is the strongest for the (400)-reflection of GaAs (Bragg angle, 76.4°).

© Author(s) 2019

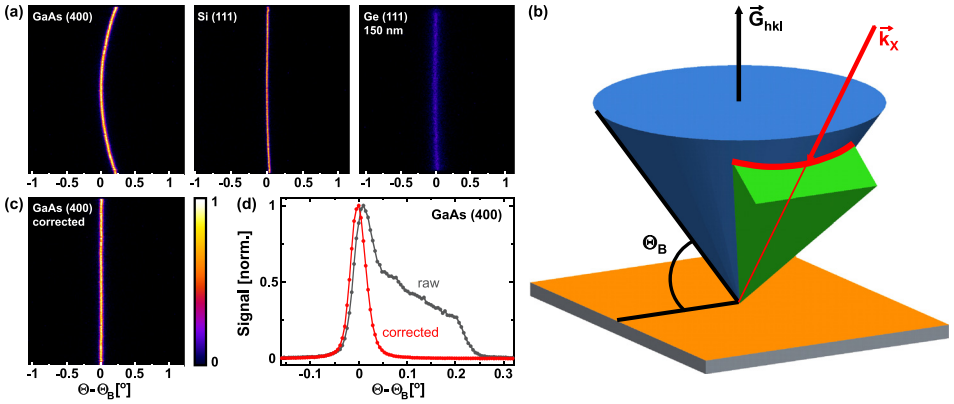

FIG. 6. (a) Raw detector images of (i) the (400)-reflection of a (100)-oriented GaAs-crystal, (ii) the (111)-reflection of a (111)-oriented Si-crystal, and (iii) the (111)-reflection of a 180 nm thick, (111)-oriented Ge film grown on the Si crystal. (b) Schematic of diffraction geometry. Blue: Kossel-cone corresponding to Bragg-reflection $\vec{G}_{hkl}$. Green: cone of X-rays directed to the bent crystal mirror onto the sample with the center ray $\vec{k}_X$ adjusted that it fulfills the Bragg-condition and lies, therefore, on the Kossel-cone. Red curve: line of intersection between the Kossel-cone and the cone of incident X-rays. (c) Diffraction image of the GaAs (400)-reflection after bending correction. (d) Angular dependence of the diffraction signal obtained by the vertical integration of the diffraction images without (dark gray) and with (red) bending correction.

In these images, the horizontal axis corresponds to the "dispersive" direction, and rocking curves are, in principle, obtained as horizontal cross sections after the vertical integration of the diffraction pattern. However, the bending of the diffraction pattern leads to distortions of the rocking curves. Therefore, to achieve the highest possible angular resolution, we applied a bending correction by fitting the curved diffraction line by a parabola, which is then used to "unbend" the whole pattern, e.g., Fig. 6(c). The effect and the necessity for this bending correction are illustrated in Fig. 6(d), which shows the rocking curve of the GaAs (400) reflection without (gray curve) and with (red curve) bending correction. The rocking curve obtained from the uncorrected diffraction pattern is broadened and strongly asymmetrically deformed compared to the corrected case.

Figure 7 shows (red-gray) the rocking curves derived from the measured diffraction pattern in Fig. 6 after bending correction. The experimental curves are compared to calculated rocking curves (blue) using the XCrystal-routine from the XOP-package[82] (ver. 2.3).

It is obvious that all experimental curves exhibit a larger width than the curves calculated for perfect crystals and a strictly monochromatic and fully collimated X-ray beam. The experimental rocking curve width $\Delta\Theta_{exp}$ has three different contributions, namely, due to the finite X-ray spot size (converted into angle) on the sample $\Delta\Theta_{spot}$, due to the bandwidth of the radiation reflected by the bent mirror $\Delta\Theta_{bw}$, and due to the "natural" rocking curve width $\Delta\Theta_{rc}$ of the corresponding reflection (polarization averaged). We assume here $\Delta\Theta^2_{exp} = \Delta\Theta^2_{spot} + \Delta\Theta^2_{bw} + \Delta\Theta^2_{rc}$.

Commercial wafers of GaAs and Si, as have been used here, exhibit almost a perfect crystalline structure. Therefore, their natural rocking curve should be close to the calculated ones. For the Si (111)-reflection, we measure an angular width of $\Delta\Theta^{Si}_{tot} = 0.022°$ corresponding to 4 pixels or 80 μm on the detector and thus equal to the measured X-ray spot size on the sample [compare Fig. 5(b)]. In this case, the contributions from the natural rocking curve width $\Delta\Theta_{rc} = 0.003°$ and the bandwidth $\Delta\Theta_{bw} = 0.003°$ (see below) are negligible. In contrast, for the case of the thin Ge-film, $\Delta\Theta_{rc}$ dominates the overall width. However, the measured width of 0.074° is significantly larger than the width of the calculated rocking curve (0.04°). Moreover, the experimental rocking curve lacks the thickness fringes of the calculated curve. We attribute both observations to a finite mosaic spread in the hetero-epitaxially grown film. Finally, for the GaAs (400)-reflection, all three effects contribute similarly, which allows us to determine the spectral bandwidth of the radiation reflected by the mirror. With a total

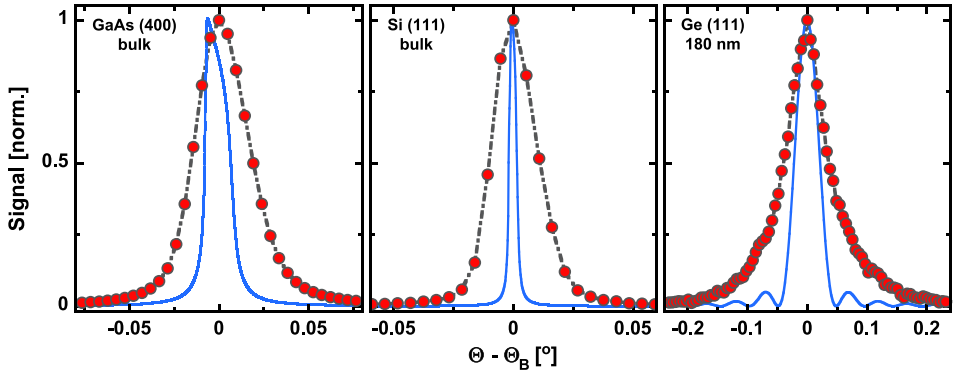

FIG. 7. Rocking curves of the GaAs (400)-reflection [bulk crystal, left, same data as in Fig. 6(d)], the Si (111)-reflection (bulk, middle), and the Ge (111)-reflection (180 nm film, right). Red-gray: experimental data after bending correction and blue: calculated rocking curves using the XCrystal-routine from the XOP-package[82] (ver. 2.3).

© Author(s) 2019

width of $\Delta\Theta_{tot} = 0.034°$, a spot size contribution of $\Delta\Theta_{spot} = 0.019°$, and a natural rocking curve width of $\Delta\Theta_{rc} = 0.015°$, a bandwidth contribution of $\Delta\Theta_{bw} = 0.023°$ is obtained. This results in an energy bandwidth of $\Delta E_{mi} = \frac{\Delta\theta_{bw}}{\tan\theta_B} E_X \approx 0.43$ eV ($\theta_B = 76.5°$ GaAs (400) Bragg angle; $E_X = 4.51$ keV X-ray photon energy) or a relative bandwidth of $\approx 10^{-4}$. This bandwidth is comparable but larger than the natural bandwidth of the Ge (400)-reflection of a plane crystal of $\Delta E_{rc} = 0.27$ eV. We attribute this to slight strain effects in the bent crystal, which will increase its bandwidth and decrease the peak reflectivity.[83]

With the mirror bandwidth $\Delta E_{mi} = 0.43$ eV, its acceptance solid angle $\Delta\Omega_{mi} = 1.92 \times 10^{-3}$ sr, assuming a polarization-averaged peak reflectivity $R_{av} = 0.85$ (chosen somewhat smaller than the value of 0.92 for the plane crystal), and the measured Ti-$K_{\alpha 1}$ linewidth of $\Delta E_{K_{\alpha 1}} = 3.1$ eV, we can derive the mirror efficiency as $\eta = R_{av} \cdot (\Delta E_{mi}/\Delta E_{K_{\alpha 1}}) \cdot (\Delta\Omega_{mi}/4\pi) \approx 1.8 \times 10^{-5}$ (this value has been used to estimate the total K_α-yield of our plasma X-ray source; see Sec. III B).

We finally present here exemplary time-resolved data obtained on the Ge/Si heterostructure after optical excitation of the Ge top layer with 100 fs, 800 nm laser pulses. Figure 8 shows the measured transient rocking curves (red) of the (111)-reflection of the 180 nm Ge overlayer (left column, linear scale) and the (111)-reflection of the bulk Si-substrate (right column, logarithmic scale) for three different pump-probe time delays. The gray curves represent the corresponding rocking curves of the unexcited sample measured at a pump-probe time delay of −15 ps, i.e., before the arrival of the optical pump.

For the Ge film, we observe a shift and broadening of the whole rocking curve toward smaller diffraction angles, indicating (an initially inhomogeneous) expansion of the lattice. In contrast, the main peak of the Si-rocking curve remains essentially unchanged but develops shoulders, initially only on the high angle side (indicating compression), but later also on the low-angle side (indicating expansion). This behavior can be explained by strain waves,[84] which are triggered by the almost instantaneous increase in stress/pressure in the Ge-film upon its electronic excitation and the subsequent lattice heating.

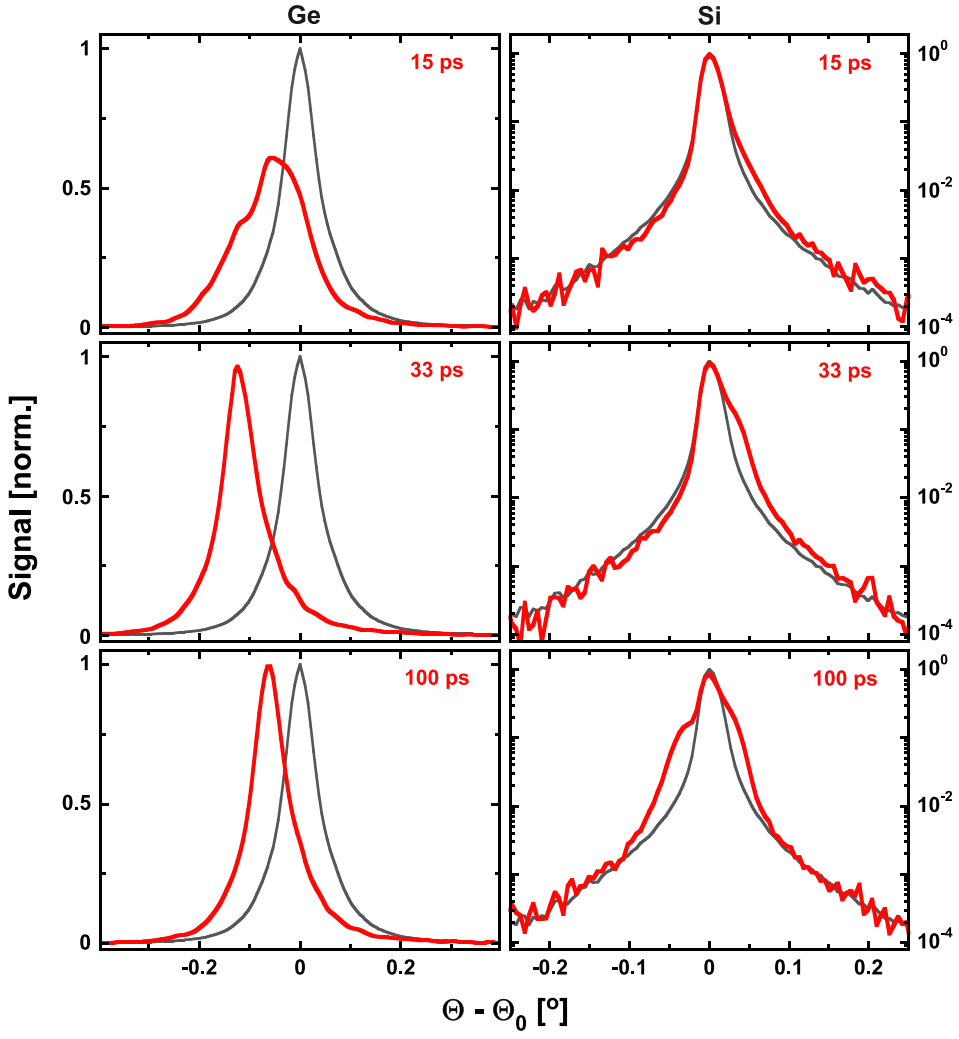

FIG. 8. Transient rocking curves (red) of the (111) Bragg reflection of (i) a 180 nm Ge film (left, linear scale) and (ii) the (111)-reflection of the bulk Si substrate (right, logarithmic scale) for different pump-probe delay times. Gray curves: experimental data measured at $\Delta t = -15$ ps as reference. Red curves: experimental data at different delays.

© Author(s) 2019

Initially, rarefaction waves are launched at both boundaries of the Ge film (the free surface and the Ge-Si interface), which propagate back and forth in the Ge-film while being partially transmitted into the Si-substrate on each round trip. The expansion of the Ge-film is evidenced by the overall shift (and broadening) of the rocking curves toward smaller diffraction angles. This expansion leads to a compression of the Si substrate (shoulder of the Si rocking curve on the high angle side for 15 ps and 33 ps). At later times, a train of bipolar strain pulses[14,84,85] develops, resulting in shoulders/satellites on both sides of the main Si (111)-peak.

The detailed strain evolution is determined by the complex interplay of electronic and thermal stress contributions,[84] which, as our measurements reveal, exhibit pronounced temporal and fluence dependencies. This we attribute to the dependence of the effective deformation potential, which determines the magnitude of the electronic stress, on the fluence- and time-dependent density of the laser-excited electron-hole plasma. While a detailed discussion of these processes is beyond the scope of this paper and will be presented in a separate publication,[86] we would like to stress that the high dynamic range (best visible for the logarithmically presented Si-data) of almost 10^4 enabled us to monitor even subtle changes in the rocking curves with high sensitivity and was key to separate and quantify different stress contributions.

IV. DISCUSSION AND SUMMARY

In summary, we have presented here a modular setup for time-resolved "optical-pump—X-ray-probe" diffraction experiments, which is based on a low repetition rate (10 Hz), laser-driven plasma K_α X-ray source. X-ray production with Ti as the target material has been optimized by carefully adjusting the laser intensity and by employing a prepulse-scheme resulting in a total Ti K_α (4.51 keV) flux of up to 1.7×10^{11} photons per second into the full solid angle. By using a toroidally bent Ge (100) crystal to collect and refocus the K_α emission of the plasma, narrow bandwidth (0.43 eV; 10^{-4} relative) radiation with $\approx 2 \times 10^6$ photons per second and a small spot size of $\approx 80\,\mu$m (FWHM) can be delivered to the sample. Table I summarizes the characteristics of the setup.[88]

The current configuration, by using the bent crystal optics, allows experiments with high angular/momentum resolution and is—as demonstrated by the data presented in Fig. 8—well suited to monitor the transient changes in rocking curves. However, the modular approach provides a high flexibility to adopt the setup to specific requirements of a particular experiment/application: (i) The target material defines the X-ray photon energy, and we use our wire-source also with Cu ($E_{K\alpha} = 8.05$ keV) since suitable X-ray optics (bent crystals[59] and multilayer optics[75,76]) are available. (ii) Using multilayer optics, which exhibit a significantly larger bandwidth (i.e., full K_α emission), we can expect with our current source an almost an order-of-magnitude higher K_α photon flux on the sample. Such a configuration can be used when the shape and position of the rocking curve do not change, but only the diffraction intensity due to the structure factor changes (e.g., caused by the excitation of optical phonons[18,89]). (iii) Also, the sample environment can be flexibly changed to allow for example measurements at low temperatures (cryostat) or the study of irreversible dynamics (e.g., melting[15–17]), which require a sample manipulator/goniometer for large samples (≈10 cm) and rapid sample motion since a fresh sample area has to be provided for each pulse.

TABLE I. Summary of the setup properties.

Parameter	Value
Laser wavelength	800 nm
Laser pulse duration	100 fs
Repetition rate	10 Hz
Main-pulse intensity (max.)/ diameter (focus)	$\sim 10^{17}$ Wcm^{-2}/$\sim$25 μm (FWHM)
Pre-pulse intensity (max.)/diameter (focus)	$\sim 10^{15}$ Wcm^{-2}/$\sim$60 μm (FWHM)
Optimum delay between main- and pre-pulse	∼20 ps
Ti-K_α yield	$\sim 1.3 \times 10^{10}$ photons s^{-1} sr^{-1}
Bent mirror spectral bandwidth/ relative bandwidth[a]	∼0.43 eV/$\lesssim 10^{-4}$
Bent mirror efficiency	$\sim 1.8 \times 10^{-5}$
X-ray convergence angle (horizontal /vertical)	1.4°/4.5°
X-ray focal spot diameter	∼80 μm (FWHM)
Average X-ray spectral brightness[87] (in the focus)	$\sim 2 \times 10^6$ Photons s^{-1} mm^{-2} mrad^{-2} (0.1% bandwidth)$^{-1}$

[a]Centered at Ti-$K_{\alpha 1} \equiv 4.51$ keV.

It also needs be stressed that many other laser plasma X-ray sources employ few-millijoule, kilohertz repetition rate laser systems and achieve a similar average X-ray flux. In contrast, we use a high pulse energy (>100 mJ), low repetition rate drive laser, which results in a two orders of magnitude higher per-pulse X-ray flux. Therefore, a correspondingly lower number of X-ray probe- and optical pump cycles is required to obtain time-resolved diffraction data with a similar integrated signal. This reduction of the optical "dose" is critical for the above-mentioned studies of irreversible dynamics since the sample area is usually limited and more generally when working in an excitation regime where accumulative sample damage becomes an issue.

ACKNOWLEDGMENTS

Financial support by the Deutsche Forschungsgemeinschaft (DFG, German Research Foundation) through project C01 "Structural Dynamics in Impulsively Excited Nanostructures" of the Collaborative Research Center SFB 1242 "Non-Equilibrium Dynamics of Condensed Matter in the Time Domain" (Project No. 278162697) is gratefully acknowledged. The authors thank M. Horn-von Hoegen, M. Kammler, and T. Wietler for providing the Ge-Si-heterostructure used in this work.

REFERENCES

[1]T. Elsaesser and M. Woerner, "Perspective: Structural dynamics in condensed matter mapped by femtosecond x-ray diffraction," J. Chem. Phys. **140**, 020901 (2014).
[2]R. J. D. Miller, "Femtosecond crystallography with ultrabright electrons and x-rays: Capturing chemistry in action," Science **343**, 1108 (2014).

© Author(s) 2019

[3]S. P. Weathersby, G. Brown, M. Centurion, T. F. Chase, R. Coffee, J. Corbett, J. P. Eichner, J. C. Frisch, A. R. Fry, M. Gühr, N. Hartmann, C. Hast, R. Hettel, R. K. Jobe, E. N. Jongewaard, J. R. Lewandowski, R. K. Li, A. M. Lindenberg, I. Makasyuk, J. E. May, D. McCormick, M. N. Nguyen, A. H. Reid, X. Shen, K. Sokolowski-Tinten, T. Vecchione, S. L. Vetter, J. Wu, J. Yang, H. A. Dürr, and X. J. Wang, "Mega-electron-volt ultrafast electron diffraction at SLAC national accelerator laboratory," Rev. Sci. Instrum. **86**, 073702 (2015).
[4]R. Schoenlein, T. Elsaesser, K. Holldack, Z. Huang, H. Kapteyn, M. Murnane, and M. Woerner, "Recent advances in ultrafast x-ray sources," Philos. Trans. R. Soc., A **377**, 20180384 (2019).
[5]C. Bostedt, S. Boutet, D. M. Fritz, Z. Huang, H. J. Lee, H. T. Lemke, A. Robert, W. F. Schlotter, J. J. Turner, and G. J. Williams, "Linac coherent light source: The first five years," Rev. Mod. Phys. **88**, 015007 (2016).
[6]A. Krol, A. Ikhlef, J. C. Kieffer, D. A. Bassano, C. C. Chamberlain, Z. Jiang, H. Pépin, and S. C. Prasad, "Laser-based microfocused x-ray source for mammography: Feasibility study," Med. Phys. **24**, 725 (1997).
[7]R. Toth, S. Fourmaux, T. Ozaki, M. Servol, J. C. Kieffer, R. E. Kincaid, and A. Krol, "Evaluation of ultrafast laser-based hard x-ray sources for phase-contrast imaging," Phys. Plasmas **14**, 053506 (2007).
[8]L. Chen, W. Wang, M. Kando, L. Hudson, F. Liu, X. Lin, J. Ma, Y. Li, S. Bulanov, T. Tajima, Y. Kato, Z. Sheng, and J. Zhang, "High contrast femtosecond laser-driven intense hard x-ray source for imaging application," in Frontiers in radiation physics and applications: Proceedings of the 11th International Symposium on Radiation Physics [Nucl. Instrum. Methods Phys. Res., Sect. A **619**, 128 (2010)].
[9]F. Ráksi, K. R. Wilson, Z. Jiang, A. Ikhlef, C. Y. Côté, and J. Kieffer, "Ultrafast x-ray absorption probing of a chemical reaction," J. Chem. Phys. **104**, 6066 (1996).
[10]C. Reich, C. M. Laperle, X. Li, B. Ahr, F. Benesch, and C. G. Rose-Petruck, "Ultrafast x-ray pulses emitted from a liquid mercury laser target," Opt. Lett. **32**, 427 (2007).
[11]F. Dorchies, A. Lévy, C. Goyon, P. Combis, D. Descamps, C. Fourment, M. Harmand, S. Hulin, P. M. Leguay, S. Petit, O. Peyrusse, and J. J. Santos, "Unraveling the solid-liquid-vapor phase transition dynamics at the atomic level with ultrafast x-ray absorption near-edge spectroscopy," Phys. Rev. Lett. **107**, 245006 (2011).
[12]L. Miaja-Avila, G. C. O'Neil, Y. I. Joe, B. K. Alpert, N. H. Damrauer, W. B. Doriese, S. M. Fatur, J. W. Fowler, G. C. Hilton, R. Jimenez, C. D. Reintsema, D. R. Schmidt, K. L. Silverman, D. S. Swetz, H. Tatsuno, and J. N. Ullom, "Ultrafast time-resolved hard x-ray emission spectroscopy on a tabletop," Phys. Rev. X **6**, 031047 (2016).
[13]M. I. Anwar, M. Iqbal, B. J. Hwang, M. Faiyaz, B. S. Mun, K. A. Janulewicz, and D. Y. Noh, "Ultrafast x-ray absorption near edge spectroscopy of Fe_3O_4 using a laboratory based femtosecond x-ray source," Opt. Express **27**, 6030 (2019).
[14]C. Rose-Petruck, R. Jimenez, T. Guo, A. Cavalleri, C. W. Siders, F. Rksi, J. A. Squier, B. C. Walker, K. R. Wilson, and C. P. J. Barty, "Picosecond-milliångström lattice dynamics measured by ultrafast x-ray diffraction," Nature **398**, 310 (1999).
[15]C. W. Siders, A. Cavalleri, K. Sokolowski-Tinten, C. Tóth, T. Guo, M. Kammler, M. H. V. Hoegen, K. R. Wilson, D. V. D. Linde, and C. P. J. Barty, "Detection of nonthermal melting by ultrafast x-ray diffraction," Science **286**, 1340 (1999).
[16]A. Rousse, C. Rischel, S. Fourmaux, I. Uschmann, S. Sebban, G. Grillon, P. Balcou, E. Förster, J. P. Geindre, P. Audebert, J. C. Gauthier, and D. Hulin, "Non-thermal melting in semiconductors measured at femtosecond resolution," Nature **410**, 65 (2001).
[17]K. Sokolowski-Tinten, C. Blome, C. Dietrich, A. Tarasevitch, M. Horn von Hoegen, D. von der Linde, A. Cavalleri, J. Squier, and M. Kammler, "Femtosecond x-ray measurement of ultrafast melting and large acoustic transients," Phys. Rev. Lett. **87**, 225701 (2001).
[18]K. Sokolowski-Tinten, C. Blome, J. Blums, A. Cavalleri, C. Dietrich, A. Tarasevitch, I. Uschmann, E. Förster, M. Kammler, M. Horn-von Hoegen, and D. von der Linde, "Femtosecond x-ray measurement of coherent lattice vibrations near the Lindemann stability limit," Nature **422**, 287 (2003).
[19]M. Bargheer, N. Zhavoronkov, Y. Gritsai, J. C. Woo, D. S. Kim, M. Woerner, and T. Elsaesser, "Coherent atomic motions in a nanostructure studied by femtosecond x-ray diffraction," Science **306**, 1771 (2004).
[20]C. v Korff Schmising, M. Bargheer, M. Kiel, N. Zhavoronkov, M. Woerner, T. Elsaesser, I. Vrejoiu, D. Hesse, and M. Alexe, "Coupled ultrafast lattice and polarization dynamics in ferroelectric nanolayers," Phys. Rev. Lett. **98**, 257601 (2007).
[21]F. Quirin, M. Vattilana, U. Shymanovich, A.-E. El-Kamhawy, A. Tarasevitch, J. Hohlfeld, D. von der Linde, and K. Sokolowski-Tinten, "Structural dynamics in FeRh during a laser-induced metamagnetic phase transition," Phys. Rev. B **85**, 020103 (2012).
[22]J. Stingl, F. Zamponi, B. Freyer, M. Woerner, T. Elsaesser, and A. Borgschulte, "Electron transfer in a virtual quantum state of $LiBH_4$ induced by strong optical fields and mapped by femtosecond x-ray diffraction," Phys. Rev. Lett. **109**, 147402 (2012).
[23]V. Juvé, M. Holtz, F. Zamponi, M. Woerner, T. Elsaesser, and A. Borgschulte, "Field-driven dynamics of correlated electrons in LiH and $NaBH_4$ revealed by femtosecond x-ray diffraction," Phys. Rev. Lett. **111**, 217401 (2013).
[24]J. Pudell, A. A. Maznev, M. Herzog, M. Kronseder, C. H. Back, G. Malinowski, A. von Reppert, and M. Bargheer, "Layer specific observation of slow thermal equilibration in ultrathin metallic nanostructures by femtosecond x-ray diffraction," Nat. Commun. **9**, 3335 (2018).
[25]C. Rischel, A. Rousse, I. Uschmann, P.-A. Albouy, J.-P. Geindre, P. Audebert, J.-C. Gauthier, E. Fröster, J.-L. Martin, and A. Antonetti, "Femtosecond time-resolved x-ray diffraction from laser-heated organic films," Nature **390**, 490 (1997).
[26]P. Gibbon, *Short Pulse Laser Interactions with Matter: An Introduction* (Imperial College Press, 2005).
[27]D. Kühlke, U. Herpers, and D. von der Linde, "Soft x-ray emission from subpicosecond laser-produced plasmas," Appl. Phys. Lett. **50**, 1785 (1987).
[28]M. M. Murnane, H. C. Kapteyn, M. D. Rosen, and R. W. Falcone, "Ultrafast x-ray pulses from laser-produced plasmas," Science **251**, 531 (1991).
[29]F. Brunel, "Not-so-resonant, resonant absorption," Phys. Rev. Lett. **59**, 52 (1987).
[30]P. Gibbon and A. R. Bell, "Collisionless absorption in sharp-edged plasmas," Phys. Rev. Lett. **68**, 1535 (1992).
[31]U. Teubner, J. Bergmann, B. van Wonterghem, F. P. Schäfer, and R. Sauerbrey, "Angle-dependent x-ray emission and resonance absorption in a laser-produced plasma generated by a high intensity ultrashort pulse," Phys. Rev. Lett. **70**, 794 (1993).
[32]U. Teubner, P. Gibbon, E. Förster, F. Falliès, P. Audebert, J. P. Geindre, and J. C. Gauthier, "Subpicosecond KrF*-laser plasma interaction at intensities between 10^{14} and 10^{17} W/cm2," Phys. Plasmas **3**, 2679 (1996).
[33]U. Teubner, W. Theobald, and C. Wülker, "Mechanisms and origin of continuum and line emission from carbon plasmas produced by ultrashort laser pulses," J. Phys. B **29**, 4333 (1996).
[34]C. Reich, P. Gibbon, I. Uschmann, and E. Förster, "Yield optimization and time structure of femtosecond laser plasma K_α sources," Phys. Rev. Lett. **84**, 4846 (2000).
[35]C. Ziener, I. Uschmann, G. Stobrawa, C. Reich, P. Gibbon, T. Feurer, A. Morak, S. Düsterer, H. Schwoerer, E. Förster, and R. Sauerbrey, "Optimization of K_α bursts for photon energies between 1.7 and 7 keV produced by femtosecond-laser-produced plasmas of different scale length," Phys. Rev. E **65**, 066411 (2002).
[36]C. Reich, I. Uschmann, F. Ewald, S. Düsterer, A. Lübcke, H. Schwoerer, R. Sauerbrey, E. Förster, and P. Gibbon, "Spatial characteristics of K_α x-ray emission from relativistic femtosecond laser plasmas," Phys. Rev. E **68**, 056408 (2003).
[37]J. Weisshaupt, V. Juvé, M. Holtz, M. Woerner, and T. Elsaesser, "Theoretical analysis of hard x-ray generation by nonperturbative interaction of ultrashort light pulses with a metal," Struct. Dyn. **2**, 024102 (2015).
[38]A. Rousse, P. Audebert, J. P. Geindre, F. Falliès, J. C. Gauthier, A. Mysyrowicz, G. Grillon, and A. Antonetti, "Efficient K_α x-ray source from femtosecond laser-produced plasmas," Phys. Rev. E **50**, 2200 (1994).
[39]F. Zamponi, Z. Ansari, M. Woerner, and T. Elsaesser, "Femtosecond powder diffraction with a laser-driven hard x-ray source," Opt. Express **18**, 947 (2010).
[40]C. J. Powell, "Cross sections for ionization of inner-shell electrons by electrons," Rev. Mod. Phys. **48**, 33 (1976).
[41]F. Ewald, H. Schwoerer, and R. Sauerbrey, "K_α radiation from relativistic laser-produced plasmas," Europhys. Lett. **60**, 710 (2002).

© Author(s) 2019

[42]D. C. Eder, G. Pretzler, E. Fill, K. Eidmann, and A. Saemann, "Spatial characteristics of K_α radiation from weakly relativistic laser plasmas," Appl. Phys. B **70**, 211 (2000).
[43]D. D. Meyerhofer, H. Chen, J. A. Delettrez, B. Soom, S. Uchida, and B. Yaakobi, "Resonance absorption in high-intensity contrast, picosecond laser-plasma interactions," Phys. Fluids B **5**, 2584 (1993).
[44]Z. Jiang, J. C. Kieffer, J. P. Matte, M. Chaker, O. Peyrusse, D. Gilles, G. Korn, A. Maksimchuk, S. Coe, and G. Mourou, "X-ray spectroscopy of hot solid density plasmas produced by subpicosecond high contrast laser pulses at 10^{18} – 10^{19} W/cm^2," Phys. Plasmas **2**, 1702 (1995).
[45]P. Gibbon and E. Förster, "Short-pulse laser-plasma interactions," Plasma Phys. Controlled Fusion **38**, 769 (1996).
[46]T. Feurer, A. Morak, I. Uschmann, C. Ziener, H. Schwoerer, E. Förster, and R. Sauerbrey, "An incoherent sub-picosecond x-ray source for time-resolved x-ray-diffraction experiments," Appl. Phys. B **72**, 15 (2001).
[47]J. Weisshaupt, V. Juvé, M. Holtz, S. Ku, M. Woerner, T. Elsaesser, S. Ališauskas, A. Pugžlys, and A. Baltuška, "High-brightness table-top hard x-ray source driven by sub-100-femtosecond mid-infrared pulses," Nat. Photonics **8**, 927 (2014).
[48]S. Fourmaux and J. C. Kieffer, "Laser-based K_α x-ray emission characterization using a high contrast ratio and high-power laser system," Appl. Phys. B **122**, 162 (2016).
[49]Y. Azamoum, R. Clady, A. Ferré, M. Gambari, O. Utéza, and M. Sentis, "High photon flux K_α Mo x-ray source driven by a multi-terawatt femtosecond laser at 100 Hz," Opt. Lett. **43**, 3574 (2018).
[50]Y. Azamoum, V. Tcheremiskine, R. Clady, A. Ferré, L. Charmasson, O. Utéza, and M. Sentis, "Impact of the pulse contrast ratio on Molybdenum K_α generation by ultrahigh intensity femtosecond laser solid interaction," Sci. Rep. **8**, 4119 (2018).
[51]N. Zhavoronkov, Y. Gritsai, M. Bargheer, M. Woerner, and T. Elsaesser, "Generation of ultrashort K_α radiation from quasipoint interaction area of femtosecond pulses with thin foils," Appl. Phys. Lett. **86**, 244107 (2005).
[52]F. Y. Khattak, O. A. M. B. Percie du Sert, D. Riley, P. S. Foster, E. J. Divall, C. J. Hooker, A. J. Langley, J. Smith, and P. Gibbon, "Comparison of experimental and simulated K_α yield for 400 nm ultrashort pulse laser irradiation," Phys. Rev. E **74**, 027401 (2006).
[53]S. Bastiani, A. Rousse, J. P. Geindre, P. Audebert, C. Quoix, G. Hamoniaux, A. Antonetti, and J. C. Gauthier, "Experimental study of the interaction of subpicosecond laser pulses with solid targets of varying initial scale lengths," Phys. Rev. E **56**, 7179 (1997).
[54]T. Schlegel, S. Bastiani, L. Grémillet, J.-P. Geindre, P. Audebert, J.-C. Gauthier, E. Lefebvre, G. Bonnaud, and J. Delettrez, "Comparison of measured and calculated x-ray and hot-electron production in short-pulse laser-solid interactions at moderate intensities," Phys. Rev. E **60**, 2209 (1999).
[55]H. Nakano, T. Nishikawa, and N. Uesugi, "Enhanced K-shell x-ray line emissions from aluminum plasma created by a pair of femtosecond laser pulses," Appl. Phys. Lett. **79**, 24 (2001).
[56]K. Sokolowski-Tinten, C. Blome, J. Blums, A. Cavalleri, C. Dietrich, A. Tarasevitch, and D. von der Linde, "Ultrafast time-resolved x-ray diffraction," AIP Conf. Proc. **634**, 11 (2002).
[57]W. Lu, M. Nicoul, U. Shymanovich, A. Tarasevitch, P. Zhou, K. Sokolowski-Tinten, D. von der Linde, M. Mašek, P. Gibbon, and U. Teubner, "Optimized K_α x-ray flashes from femtosecond-laser-irradiated foils," Phys. Rev. E **80**, 026404 (2009).
[58]T. Missalla, I. Uschmann, E. Förster, G. Jenke, and D. von der Linde, "Monochromatic focusing of subpicosecond x-ray pulses in the keV range," Rev. Sci. Instrum. **70**, 1288 (1999).
[59]M. Nicoul, U. Shymanovich, S. Kähle, T. Caughey, D. Sampat, K. Sokolowski-Tinten, and D. von der Linde, "Bent crystal x-ray mirrors for time-resolved experiments with femtosecond laser-produced x-ray pulses," J. Phys.: Conf. Ser. **21**, 207 (2005).
[60]B. Henke, E. Gullikson, and J. Davis, "X-ray interactions: Photoabsorption, scattering, transmission, and reflection at E=50–30000 eV, Z=1–92," At. Data Nucl. Data Tables **54**, 181 (1993).
[61]The quantum efficiency of the CCD was measured with a calibrated Si reference detector (Amptek XR100-CR).
[62]D. Schick, A. Bojahr, M. Herzog, C. V. K. Schmising, R. Shayduk, W. Leitenberger, P. Gaal, and M. Bargheer, "Normalization schemes for ultrafast x-ray diffraction using a table-top laser-driven plasma source," Rev. Sci. Instrum. **83**, 025104 (2012).
[63]B. B. Zhang, S. S. Sun, D. R. Sun, and Y. Tao, "Note: A novel normalization scheme for laser-based plasma x-ray sources," Rev. Sci. Instrum. **85**, 096110 (2014).
[64]S. Höfer, T. Kämpfer, E. Förster, T. Stöhlker, and I. Uschmann, "Communication: The formation of rarefaction waves in semiconductors after ultrashort excitation probed by grazing incidence ultrafast time-resolved x-ray diffraction," Struct. Dyn. **3**, 051101 (2016).
[65]M. Holtz, C. Hauf, J. Weisshaupt, A.-A. H. Salvador, M. Woerner, and T. Elsaesser, "Towards shot-noise limited diffraction experiments with table-top femtosecond hard x-ray sources," Struct. Dyn. **4**, 054304 (2017).
[66]F. Zamponi, T. Kämpfer, A. Morak, I. Uschmann, and E. Förster, "Characterization of a deep depletion, back-illuminated charge-coupled device in the x-ray range," Rev. Sci. Instrum. **76**, 116101 (2005).
[67]S. I. Salem and P. L. Lee, "Experimental widths of K and L x-ray lines," At. Data Nucl. Data Tables **18**, 233–241 (1976).
[68]A. Sengebusch, H. Reinholz, G. Röpke, U. Zastrau, T. Kämpfer, I. Uschmann, E. Förster, E. Stambulchik, E. Kroupp, and Y. Maron, "K-line emission profiles with focus on the self-consistent calculation of plasma polarization," J. Phys. A **42**, 214061 (2009).
[69]V. Arora, H. Singhal, P. A. Naik, and P. D. Gupta, "Conversion efficiency and spectral broadening of the K-α line emitted from planar titanium targets irradiated with ultra-short laser pulses of high intensity," J. Appl. Phys. **110**, 083305 (2011).
[70]For this measurement the CCD has been placed between the toroidal mirror and the sample and the total K_α yield was estimated by taking into account the efficiency of the bent mirror of about 1.8×10^{-5} (see Sec. III D) and that the $K_{\alpha 2}$ flux is half of the $K_{\alpha 1}$ flux [Fig. 2(b)].
[71]E. Fill, J. Bayerl, and R. Tommasini, "A novel tape target for use with repetitively pulsed lasers," Rev. Sci. Instrum. **73**, 2190 (2002).
[72]The measurements in. Figs. 3(a) and 3(b) have been performed on different days. Day-to-day variations of the source performance are responsible for the slight difference in yield measured at optimum pre- and main-pulse delay. During the lens position scan. [Blue data points in Fig. 3(a)] and the maximum yield reported in Fig. 3(b).
[73]B. Lengeler, C. G. Schroer, M. Kuhlmann, B. Benner, T. L. Günzler, O. Kurapova, F. Zontone, A. Snigirev, and I. Snigireva, "Refractive x-ray lenses," J. Phys. D: Appl. Phys. **38**, A218 (2005).
[74]H. Yumoto, H. Mimura, T. Koyama, S. Matsuyama, K. Tono, T. Togashi, Y. Inubushi, T. Sato, T. Tanaka, T. Kimura, H. Yokoyama, J. Kim, Y. Sano, Y. Hachisu, M. Yabashi, H. Ohashi, H. Ohmori, T. Ishikawa, and K. Yamauchi, "Focusing of x-ray free-electron laser pulses with reflective optics," Nat. Photonics **7**, 43 (2013).
[75]M. Bargheer, N. Zhavoronkov, R. Bruch, H. Legall, H. Stiel, M. Woerner, and T. Elsaesser, "Comparison of focusing optics for femtosecond x-ray diffraction," Appl. Phys. B **80**, 715 (2005).
[76]U. Shymanovich, M. Nicoul, K. Sokolowski-Tinten, A. Tarasevitch, C. Michaelsen, and D. von der Linde, "Characterization and comparison of x-ray focusing optics for ultrafast x-ray diffraction experiments," Appl. Phys. B **92**, 493 (2008).
[77]R. Rathore, V. Arora, H. Singhal, T. Mandal, J. A. Chakera, and P. A. Naik, "Experimental and numerical study of ultra-short laser-produced collimated Cu K_α x-ray source," Laser Part. Beams **35**, 442 (2017).
[78]M. Schollmeier, T. Ao, E. S. Field, B. R. Galloway, P. Kalita, M. W. Kimmel, D. V. Morgan, P. K. Rambo, J. Schwarz, J. E. Shores, I. C. Smith, C. S. Speas, J. F. Benage, and J. L. Porter, "Polycapillary x-ray lenses for single-shot, laser-driven powder diffraction," Rev. Sci. Instrum. **89**, 10F102 (2018).
[79]See www.inradoptics.com/pdfs/Inrad_WP_X-Ray_Toroids.pdf for "INRAD Optics, 'X-ray Toroids,' Tech. Rep."
[80]U. Shymanovich, M. Nicoul, J. Blums, K. Sokolowski-Tinten, A. Tarasevitch, T. Wietler, M. Horn von Hoegen, and D. von der Linde, "Diffraction of strongly convergent x-rays from picosecond acoustic transients," Appl. Phys. A **87**, 7 (2007).

© Author(s) 2019

[81]M. Horn-von Hoegen, M. Copel, J. C. Tsang, M. C. Reuter, and R. M. Tromp, "Surfactant-mediated growth of Ge on Si(111)," Phys. Rev. B **50**, 10811 (1994).
[82]R. J. D. Manuel Sanchez del Rio, "XOP: A multiplatform graphical user interface for synchrotron radiation spectral and optics calculations," Proc. SPIE **3152**, 148 (1997).
[83]I. Uschmann, E. Förster, K. Gäbel, G. Hölzer, and M. Ensslen, "X-ray reflection properties of elastically bent perfect crystals in Bragg geometry," J. Appl. Crystallogr. **26**, 405 (1993).
[84]C. Thomsen, H. T. Grahn, H. J. Maris, and J. Tauc, "Surface generation and detection of phonons by picosecond light pulses," Phys. Rev. B **34**, 4129 (1986).
[85]U. Shymanovich, M. Nicoul, S. Kähle, W. Lu, A. Tarsevitch, P. Zhou, T. Wietler, M. Horn-von Hoegen, D. von der Linde, and K. Sokolowski-Tinten, "The role of thermal and electronic pressure in the picosecond acoustic response of femtosecond laser-excited solids," in Online Proceedings Library Archive (2009), p. 1230.
[86]M. Afshari, U. Shymanovich, P. Krumey, M. Nicoul, D. Menn, A. Tarasevitch, T. Wietler, M. Kammler, M. Horn-von Hoegen, and K. Sokolowski-Tinten, "Picosecond acoustic response of a Ge-Si heterostructure analyzed by time-resolved X-ray diffraction" (to be published).
[87]D. M. Mills, J. R. Helliwell, Å. Kvick, T. Ohta, I. A. Robinson, and A. Authier, "Report of the working group on synchrotron radiation nomenclature—brightness, spectral brightness or brilliance?," J. Synchrotron Radiat. **12**, 385 (2005).
[88]For the setup presented here we did not characterize the X-ray pulse duration. From time-resolved diffraction experiments on Ge[17] and Bi,[18] which were carried out at earlier versions of this setup (also with a Ti wire target and pre-pulse scheme[56]) we obtained an upper boundary of about 250 fs for the X-ray pulse duration. While we do not expect the pulse duration to be significantly different here, the temporal resolution is determined by the experimental geometry (angle between X-ray probe and optical pump) to about 300–500 fs, but still sufficient to study strain wave propagation on picosecond time scales.
[89]D. M. Fritz, D. A. Reis, B. Adams, R. A. Akre, J. Arthur, C. Blome, P. H. Bucksbaum, A. L. Cavalieri, S. Engemann, S. Fahy, R. W. Falcone, P. H. Fuoss, K. J. Gaffney, M. J. George, J. Hajdu, M. P. Hertlein, P. B. Hillyard, M. Horn-von Hoegen, M. Kammler, J. Kaspar, R. Kienberger, P. Krejcik, S. H. Lee, A. M. Lindenberg, B. McFarland, D. Meyer, T. Montagne, É. D. Murray, A. J. Nelson, M. Nicoul, R. Pahl, J. Rudati, H. Schlarb, D. P. Siddons, K. Sokolowski-Tinten, T. Tschentscher, D. von der Linde, and J. B. Hastings, "Ultrafast bond softening in bismuth: Mapping a solid's interatomic potential with x-rays," Science **315**, 633 (2007).

© Author(s) 2019